

# Modulation of a dual-band metamaterial absorber in the terahertz band

Min Zhong , Xiaoting Jiang, Xuliang Zhu, Jing Zhang, Jinglin Zhong, Jin'an Chen, Shunxin Wu, Jinghao Zhang, Limian Liang, Lidan Zeng, Yulong Xin, Huixian Chen, Yuhua Chen, Shidan Huang and Kejing Yang

Hezhou University, Hezhou 542899, People's Republic of China

E-mail: [zhongmin2012hy@163.com](mailto:zhongmin2012hy@163.com)

Received 3 November 2019, revised 4 December 2019

Accepted for publication 9 December 2019

Published 24 February 2020



## Abstract

In this paper, a tunable metamaterials absorber with Dirac semimetals and VO<sub>2</sub> strips is present in the Terahertz (THz) range. At room temperature, two absorption peaks are revealed at resonance frequencies 10.1 THz (76% amplitude) and 20.3 THz (60% amplitude), respectively. Based on the tunability of these two materials, three modulation strategies are proposed to control the resonant properties of the absorber. As the conductivity increase, three newly absorption peaks (62% amplitude at 19.9 THz, 65% amplitude at 27.7 THz, and 73% amplitude at 37.3 THz) are achieved due to four VO<sub>2</sub> strips undergoing the insulation phase-metal phase changes. The resonant properties of this absorber can be converted due to the conversion function of four VO<sub>2</sub> strips. Moreover, both original absorption peaks can be control in the continuous frequency range by increasing the Fermi energy. Finally, the magnetic field external is adopted to modulate the resonant properties of this absorber. Both of the original absorption peaks are increased in a continuous frequency range, and two newly absorption peaks (74% amplitude at 23.9 THz and 60% amplitude at 36 THz) are achieved.

Keywords: metamaterials, absorption, temperature

(Some figures may appear in colour only in the online journal)

## 1. Introduction

Electromagnetic metamaterials are materials that are artificially designed and prepared for obtaining novel properties, such as superlensing, negative refraction, cloaking, and so on [1–3]. Based on these resonance properties, metamaterials are used in a variety of fields [4–6]. Metamaterial absorbers have attracted researchers' attention because of their wide applications. The absorbers are divided into different types because they exhibit different resonance properties, such as single-band absorbers, dual-band absorbers, and multi-band absorbers [7–10]. Chen *et al* designed and manufactured a fishnet structure metamaterials absorber in the microwave region, which revealed a absorption bandwidth 4.8–20.7 GHz [11]. Another polarization insensitive broadband absorber is also experimentally demonstrated based on the impedance matching condition within the operating frequency band [12]. Wu *et al* experimentally revealed a flexible water-based metamaterials absorber in the 5–25 GHz [13]. However,

resonance properties of these metamaterials absorbers can only be modulated by optimizing the structural design, which is not conducive to industrial promotion. Therefore, the design and fabrication of tunable absorbers has attracted the interest of researchers. Many tunable dielectric layers are used to develop metamaterials, such as liquid crystal, GeSbTe, or semiconductors [14–18]. Among them, vanadium dioxide (VO<sub>2</sub>) and Dirac semimetal reveal excellent tunable resonance properties [19, 20]. Recently, the 3D Dirac semimetals, which is also called '3D graphene', attract researchers' attention. This is due to the 3D Dirac semimetals is easier to be processed and more stable than the graphene layer [21]. The 3D Dirac semimetals is also revealed higher carrier mobility and lower of intrinsic loss of surface plasmon polaritons (SPPs) [22]. Moreover, the surface conductivity of Dirac semimetals can be modulated through adjusting its Fermi energy in a continuous frequency band [23]. Therefore, it is feasible to develop a continuously modulable metamaterial absorber using Dirac semimetal. Unfortunately, few

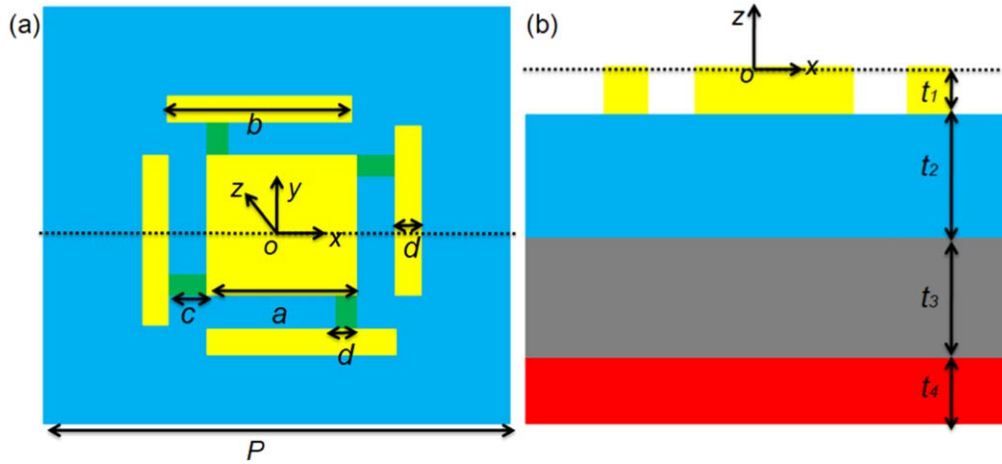


**Figure 1.** (a) The top view of the designed unit. (b) A cross section of a designed unit. The yellow parts are Dirac semimetal. The blue part is SU-8 layer. The gray part is SiO<sub>2</sub> layer. The red part is metal layer. The green parts are VO<sub>2</sub>.

**Table 1.** All of parameters of the unit cell.

Parameter	$P$	$a$	$b$	$c$	$d$	$t_1$	$t_2$	$t_3$	$t_4$
Value (nm)	2000	700	900	200	100	580	2600	1200	1100

researchers have applied both Dirac semi-metal and VO<sub>2</sub> to metamaterial absorbers. The metamaterial absorber developed with this design strategy will have the following advantages: (a) resonance properties can be continuously regulated in the target spectrum by changing the Fermi energy of the Dirac semimetal, (b) the resonance performance can be conversed due to the insulation phase-metal phase change of the VO<sub>2</sub>. Therefore, different modulation methods can be selected to meet industrial needs, and the absorber can realize continuous regulation or conversion of resonance properties. Therefore, it is meaningful to design and develop of an absorber that has both continuous regulation and property conversion functions.

In this paper, a tunable metamaterials absorber based on Dirac semimetals and VO<sub>2</sub> is designed and simulated in the THz range. Two absorption peaks are achieved at room temperature. When the simulated temperature is enhanced (the conductivity of VO<sub>2</sub> is increased), four VO<sub>2</sub> strips are revealed insulation phase-metal phase change, which results in three newly absorption peaks, while the original absorption peaks are keep unchanged. These four VO<sub>2</sub> strips correspond to the resonant nature converter of the absorber. When the Fermi energy is changed, both of original absorption peaks are modulated in a continuous frequency range. Moreover, the resonance property of the proposed absorber can also be controlled by changing the magnetic field strength in a continuous frequency range.

## 2. Structure, model and physical mechanism

The schematic diagram of the proposed unit cell can be found in figure 1. The top layer is composed of a Dirac semimetal square, four Dirac semimetal strips, and four VO<sub>2</sub> strips. Four

VO<sub>2</sub> strips are in full contact with the Dirac semimetal square and strips. The intermediate medium layer is a SU-8 layer and a SiO<sub>2</sub> layer. The bottom layer is a complete gold layer. All of specific structural parameters can be found in table 1. In this paper, the bottom gold layer is revealed as follows [24]:

$$\varepsilon_{Au} = 9 - \omega_p^2 / (\omega^2 + i\omega\gamma). \quad (1)$$

Here,  $\omega_p = 4.35\pi \times 10^{15} \text{ s}^{-1}$  is set to be the plasma frequency, and  $\gamma = 3.1916\pi \times 10^{13} \text{ s}^{-1}$  is set to be the collision frequency. The SU-8 layer and SiO<sub>2</sub> layer are revealed based on reported works [25, 26]. Ideal boundaries and perfect matching layers are applied in full-wave HFSS Ansoft [27]. The insulating region of four VO<sub>2</sub> strips is given based on the Maxwell-Garnett EMT mode [28, 29]:

$$\varepsilon_{\text{eff}}^{\text{MG}} = \varepsilon_i \frac{\varepsilon_m(1 + 2f) - \varepsilon_i(2f - 2)}{\varepsilon_i(f + 2) + \varepsilon_m(1 - f)}. \quad (2)$$

In the equation (2),  $f$  is set to be the volume fraction. And the metallic domains of four VO<sub>2</sub> strips are given based on the classical Drude model [30]:

$$\varepsilon_m = \varepsilon_\infty - \frac{\omega_p^2}{\omega(\omega + i\Gamma)} \left( 1 + \frac{ic\Gamma}{\omega + i\Gamma} \right). \quad (3)$$

In the equation (3),  $\omega_p$  is set to be the plasma frequency. And  $\omega_p^2 = Ne^2/\varepsilon_0 m^*$ ,  $\omega$  is set to be the cyclic frequency,  $\Gamma = e/m^* \mu$  is set to be the scattering rate.

Dirac semimetal square and strips are revealed based on the following model [31]:

$$\text{Re } \sigma(\Omega) = \frac{g k_F e^2}{24\pi\hbar} \Omega G \left( \frac{\Omega}{2} \right), \quad (4)$$

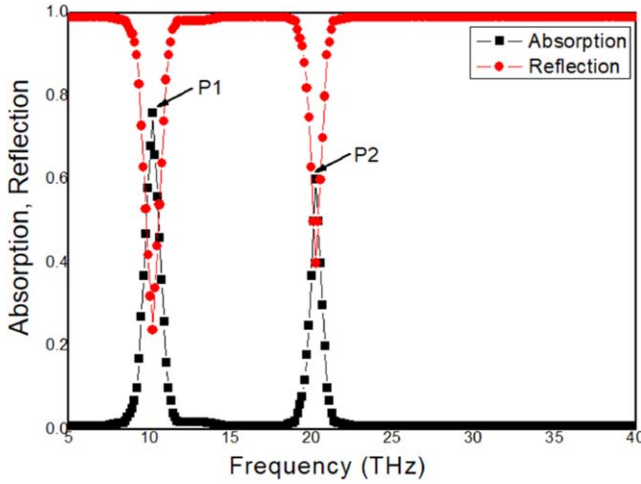


**Figure 2.** The simulated absorption spectrum with room temperature.

$$\text{Im}\sigma(\Omega) = \frac{gk_F e^2}{24\pi^2 \hbar} \left\{ \frac{4}{\Omega} \left[ 1 + \frac{\pi^2}{3} \left( \frac{T}{E_F} \right)^2 \right] + 8\Omega \int_0^{\varepsilon_c} \left[ \frac{G(\varepsilon) - G(\Omega - 2)}{\Omega^2 - 4\varepsilon^2} \right] \varepsilon d\varepsilon \right\}. \quad (5)$$

In the equations (4)–(5),  $E_F$  is set to be the Fermi level,  $G(E) = n(-E) - n(E)$  with  $n(E)$  is set to be the Fermi distribution Function.  $k_F = E_F / \hbar v_{F2}$  is set to be the Fermi momentum,  $v_{F2} = 10^6 \text{ m s}^{-1}$  is set to be the Fermi velocity.  $E_c$  is set to be the cutoff energy. Moreover,  $\varepsilon = E/E_F$ ,  $\varepsilon_c = E_c/E_F$ , and  $\Omega = \hbar\omega/E_F$ . The permittivity is given as follows [32]:

$$\varepsilon = \varepsilon_b + i\sigma/\omega\varepsilon_0. \quad (6)$$

In the equation (6),  $\varepsilon_b$  is set to be the effective background dielectric [32]. Since the bottom metal layer is thick enough, the simulated transmission is zero. Therefore, the simulated absorption can be achieved as follows:

$$A(f) = 1 - R(f). \quad (7)$$

In the equation (7),  $A(f)$  is the absorption rate,  $R(f)$  is reflection rate.

The simulated absorption spectrum is revealed in figure 2. Two absorption peaks with amplitude 76% and 60% are achieved at resonance frequencies 10.1 THz and 20.3 THz, respectively. These absorption peaks are denoted as P1 and P2, respectively. To reveal the resonance mechanism of the P1 and P2, electric field strength distribution is calculated, as shown in figure 3. At resonance frequency 10.1 THz, a surface plasmon polariton (SPP) mode is revealed on the surface of the Dirac semimetal square and two SPP modes are excited on the surface of the Dirac semimetal strips 1 and 3, as shown in figure 3(a). This is because the surface free charge of the Dirac semimetal is coupled with the electric field of the incident wave to form the SPP mode, which results in the energy loss of the electromagnetic wave in the Dirac semimetal and forms the P1 absorption peak [33], as shown in figure 3(a). At resonance frequency 20.3 THz, different from the calculation results in figure 3(a), localized

surface plasmon (LSP) modes are excited on Dirac semimetal square and strips [34]. When an electromagnetic wave is incident on the surface of the unit cell, the surface of the Dirac semimetal forms an induced current and an induced electric field. This induced conduction electrons is interacted with the incident light field in local areas of Dirac semimetal and results in these LSP modes. The energy of the electromagnetic wave is trapped and loss in these local areas of Dirac semimetal, and then excited the P2 peak [33, 34], as shown in figure 3(b).

### 3. Results and discussion

The proposed unit cell is controlled by changing Fermi energy, as shown in figure 4. The Fermi energy of Dirac semimetal square and strips is increased from 50 to 70 meV. It is found that the absorption peak P1 exhibits strong resonance behaviors. The absorption amplitude is enhanced from 76% to 86.6%, and the resonance frequency is shifted from 10.1 to 18.4 THz. However, the absorption amplitude and resonance frequency of the absorption peak P2 are changed by a small amount, as shown in figure 4. The resonance frequency shift of the P1 and P2 is due to the permittivity of Dirac semimetals is tunable due to the Fermi energy, as shown in figure 5. When the Fermi energy is increased, the real part of permittivity is reduced according to the material perturbation theory [35–37]:

$$\frac{\Delta\omega}{\omega_o} = \frac{\omega - \omega_o}{\omega_o} - \frac{\iiint_V dV [(\Delta\vec{\varepsilon} \cdot \vec{E}) \cdot \vec{E}_o + (\Delta\vec{\mu} \cdot \vec{H}) \cdot \vec{H}_o^*]}{\iiint_V dV (\varepsilon |\vec{E}_o|^2 + \mu |\vec{H}_o|^2)}. \quad (8)$$

The equation above describes the relationship between the dielectric constant and the resonant frequency. The  $\Delta\vec{\mu}$  and  $\Delta\vec{\varepsilon}$  are set to be the difference of permeability and permittivity. The  $\vec{H}_o$  and  $\vec{E}_o$  are set to be the unperturbed magnetic and electric fields. The  $\vec{H}$  and  $\vec{E}$  are set to be the perturbed magnetic and electric fields. Based on the calculated data in figure 5(b), the  $\Delta\vec{\varepsilon}$  to be negative value with the Fermi energy increasing. According to the above equation (8), the resonant frequency is shifted to higher frequencies according. Moreover, the imaginary part of permittivity is enhanced with the Fermi energy increasing, as shown in figure 5(a).

The effect of the simulated temperature on resonance properties of the proposed unit cell is revealed based on the conductivity of VO<sub>2</sub> in, as shown in figure 6. The conductivity of four VO<sub>2</sub> strips is set to be 200 S m<sup>-1</sup> in the insulation phase at room temperature. When the simulated temperature reaches or exceeds 68 °C, the conductivity is set to be  $2 \times 10^5 \text{ S m}^{-1}$ , the VO<sub>2</sub> strips undergo the insulation-metal transformation phase process. Therefore, when the conductivity of VO<sub>2</sub> reaches  $1 \times 10^6 \text{ S m}^{-1}$ , the VO<sub>2</sub> strips in the proposed unit cell reveal metal resonance properties (metal phase). Both of the amplitude and resonance frequency

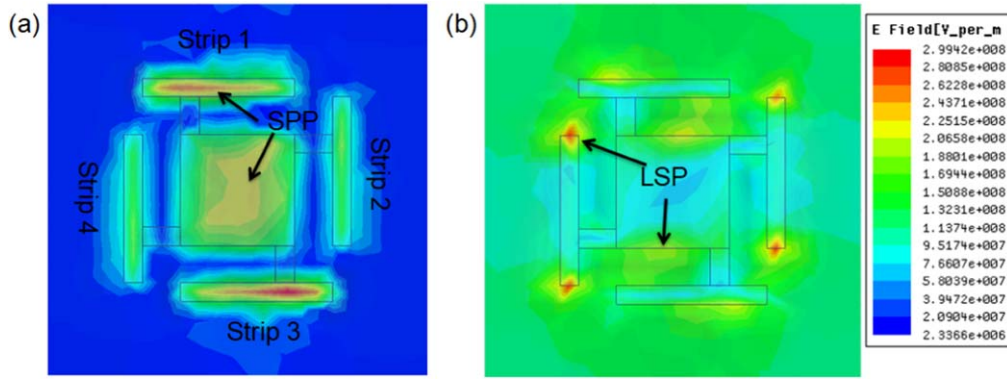


**Figure 3.** (a) The simulated electric field strength distribution at resonance frequencies 10.1 THz. (b) The simulated electric field strength distribution at resonance frequencies 20.3 THz.

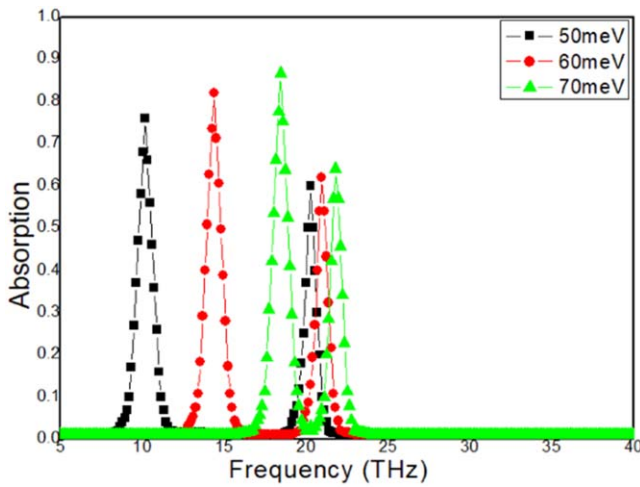


**Figure 4.** The simulated absorption spectrum with different Fermi energy.

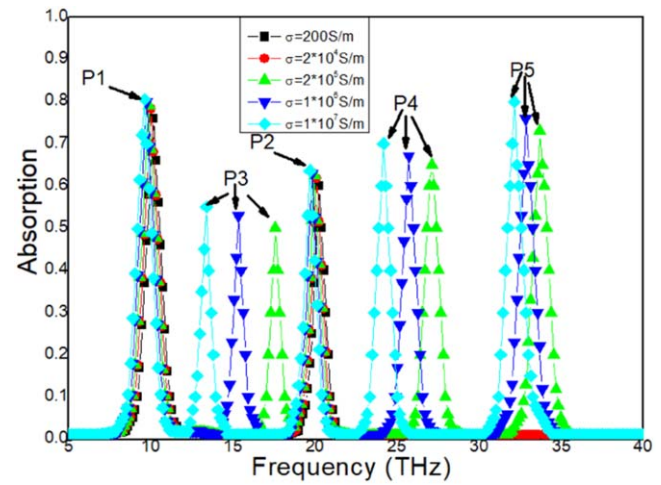


**Figure 6.** The simulated absorption spectrum with different conductivity of VO<sub>2</sub> strips.

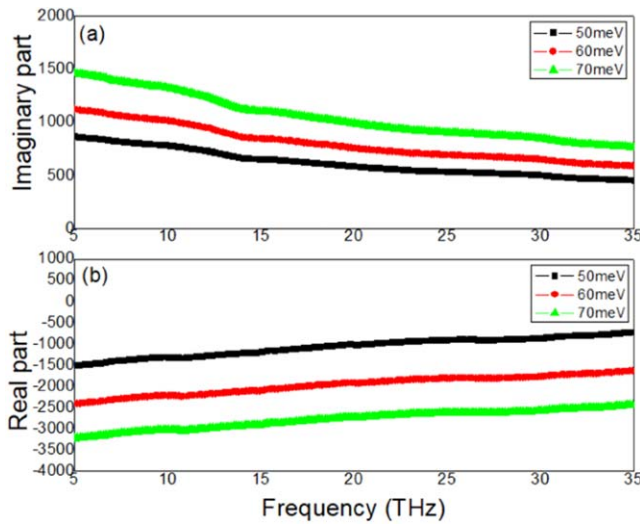


**Figure 5.** Permittivity of Dirac semimetals with different Fermi energy. (a) Imaginary parts. (b) Real parts.

of the P1 and P2 are not sensitive to the temperature change, as shown in figure 6. However, new resonance behaviors are discovered. When the conductivity of VO<sub>2</sub> strips is increased to  $2 \times 10^5 \text{ S m}^{-1}$ , three newly absorption peaks are achieved,

seen the green curve in figure 6. For ease of description, these absorption peaks are identified as P3 (62%, 19.9 THz), P4 (65%, 27.7 THz), and P5 (73%, 37.3 THz). As the conductivity increase, the amplitude of these absorption peaks (P3, P4, and P5) is enhanced and resonance frequencies are shifted to lower frequencies, as shown in figure 6. In order to find out the cause of excitation of these absorption peaks, the electric field intensity distribution is calculated, as shown in figure 7. Based on the data of the green curve, three resonance frequency points are selected. At the resonance frequency 19.9 THz, four LSP modes are excited on four VO<sub>2</sub> strips, which results in the P3 based on the metal resonance properties of VO<sub>2</sub> strips, as shown in figure 7(a). No resonant mode is excited on the surface of Dirac semimetal square and strips, as shown in figure 7(a). At the resonance frequency 27.7 THz, SPP modes are revealed on the surface of the Dirac semimetal square and two VO<sub>2</sub> strips. Moreover, LSP modes are excited on the Dirac semimetal strips 2 and 4, as shown in figure 7(b). These resonant modes are interfered and coupled together, which results in the hybridization effect in the proposed unit cell. Therefore, the absorption peak P4 is revealed by the hybridization effect between the SPP and LSP modes, as shown in figure 7(b). At the resonance frequency



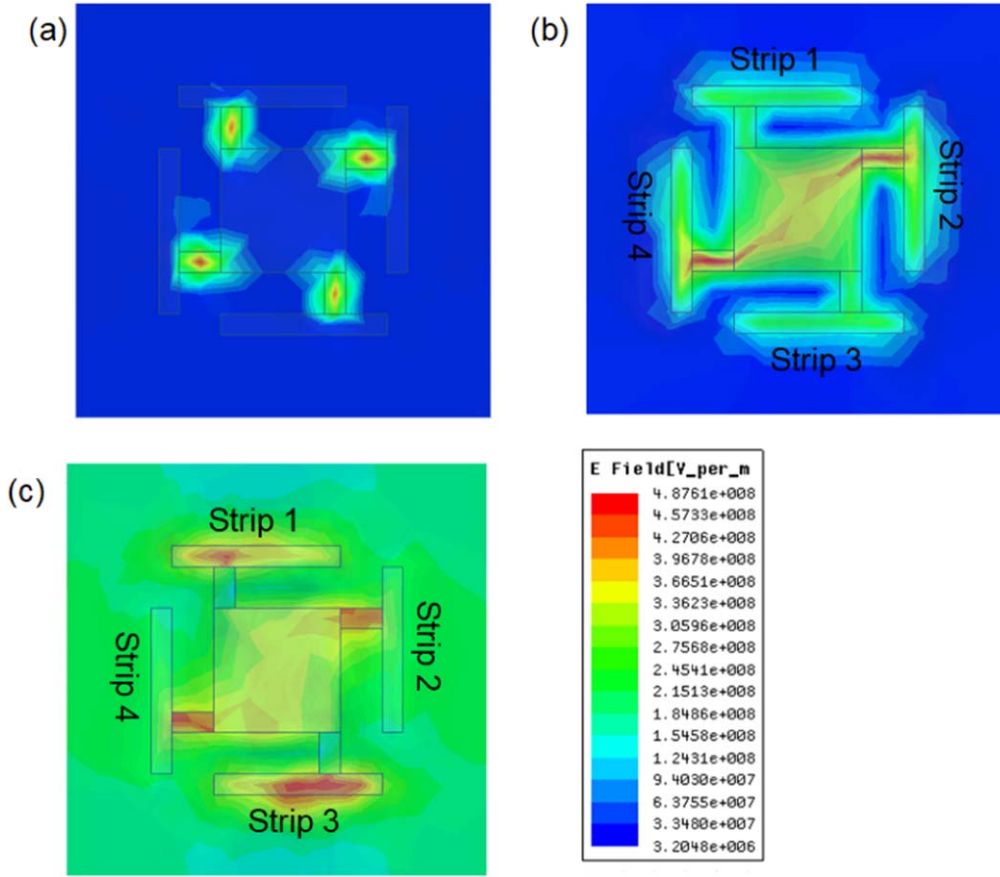


**Figure 7.** (a) Electromagnetic intensity distribution at the resonance frequency of P3 19.9 THz. (b) Electromagnetic intensity distribution at the resonance frequency of P4 27.7 THz. (c) Electromagnetic intensity distribution at the resonance frequency of P5 37.3 THz.

37.3 THz, another hybridization effect between the SPP and LSP modes is achieved in the proposed unit cell. Moreover, two LSP modes are also excited on Dirac semimetal strips 1 and 3, as shown in figure 7(b), which leads to the amplitude of the P5 is higher than that of the P4, as shown in figure 6.

The effect of the external magnetic field on the resonance properties of the proposed unit cell is revealed in figure 8. This external magnetic field can be achieved by adding additional magnetic field conditions at the boundary. When the magnetic field strength is increased from 0.0 to 0.5 T, the P1 is enhanced from 76% to 80% and the resonance frequency is shifted from 10.1 to 11.1 THz. This result shows that the external magnetic field reveals an important role on the resonance properties of the P1, as shown in figure 8. However, the amplitude and resonant frequency of the P2 are not sensitive to the applied magnetic field, even if the magnetic field strength is increased to 4.0 T, as shown in figure 8. This is due to the P2 is derived from LSP modes resonance on the surface of Dirac semimetal square and strips, as shown in figure 3. When the magnetic field strength is increased to 2.0 T, new absorption peaks are also obtained, which are labeled P6 (amplitude 74% and resonance frequency 23.9 THz) and P7 (amplitude 60% and resonance frequency 36 THz). The P6 and P7 are both enhanced and shifted to higher frequencies with the magnetic field strength increasing, as shown in figure 8. The effect of external

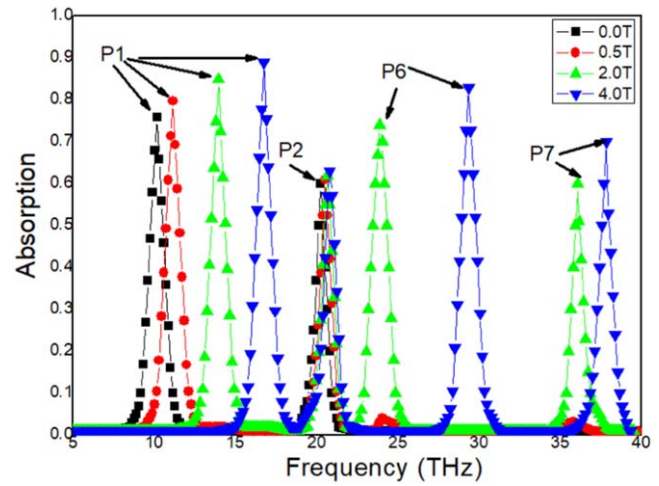


**Figure 8.** The simulated absorption spectrum with different external magnetic field.

magnetic field results in the Dirac semimetal resistance reduction due to the negative magnetoresistance effect [38]. The conductivity of the Dirac semimetal square and strips based on the magnetoresistance can be revealed as follows

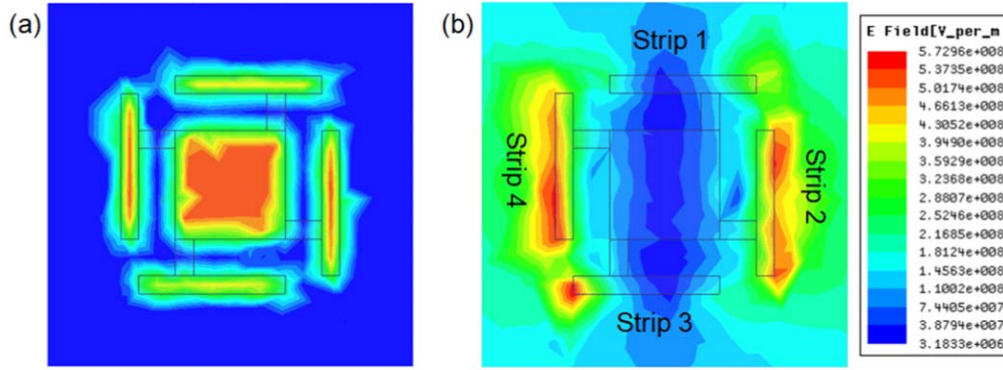


**Figure 9.** (a) Electromagnetic intensity distribution at the resonance frequency of P6 23.9 THz. (b) Electromagnetic intensity distribution at the resonance frequency of P7 36 THz.

[39–41]:

$$\Delta\sigma(B) \cong \alpha \frac{-e^2}{2\pi^2\hbar} \left[ \psi\left(\frac{1}{2} + \frac{B_\varphi}{B}\right) - \ln\left(\frac{B_\varphi}{B}\right) \right] + c \cdot B^2. \quad (9)$$

In the above equation,  $\alpha$  is set to the weak localization.  $\beta$  is set to the ratio of thickness of Dirac semimetals and mean free.  $B_\varphi = \frac{h}{4eL_\varphi}$  is set to the characteristic field. The dephasing length is  $L_\varphi$ .  $\psi(x)$  is set to the digamma function [39–41]. The surface current is enhanced due to the negative magnetoresistance effect, which leads to the SPP modes enhance and the P1 increase with the magnetic field strength increasing. Since the LSP mode is excited by the collective excitation of the edge area surface charge on Dirac semimetal square and strips, the reduction in magnetoresistance has little effect on the resonance strength of the LSP and the P2. It is obvious that the P6 and P7 are both related to the negative magnetoresistance effect, as shown in figure 8. In order to reveal the physical mechanism of the P6 and P7, the electric field intensity distribution is still calculated, as shown in figure 9. At the resonance frequency 23.9 THz, the SPP modes are revealed on the surface of Dirac semimetal square and strips based on the negative magnetoresistance effect, which leads to the P6, as shown in figure 9(a). Therefore, the P6 is sensitive to changes in the magnetic field strength, as shown in figure 8. It should be indicated that the SPP mode can not be excited on the surface of VO<sub>2</sub> strips, as shown in figure 9(a). At the resonance frequency 36 THz, two SPP modes are excited on the Dirac semimetal strips 2 and 4. At the same time, two LSP modes are also excited on the Dirac semimetal strips 1 and 3, as shown in figure 9(b). These SPP and LSP modes results in the P7. Because only the SPP mode is sensitive to the negative magnetoresistance effect, the transmission peak P7 is less sensitive to magnetic fields than P6. Both of the original absorption peaks can be continuously modulated by Fermi energy due to the permittivity of Dirac semimetals is sensitive to the Fermi energy, including amplitude and resonance frequency. It should be indicated that no new absorption peaks are obtained during the increase of Fermi energy. Three new absorption peaks can be obtained and modulated (amplitude, resonance frequency) by changing the temperature based on the insulation-metal transformation phase of the VO<sub>2</sub> strips. However, the change in temperature

has no effect on the original two absorption peaks. It is found that the two original absorption peaks can be modulated by a magnetic field. In addition, two new absorption peaks can be obtained and modulated by varying the magnetic field strength due to the negative magnetoresistance effect, as shown in figure 8.

#### 4. Conclusion

In conclusion, a tunable metamaterial absorber is numerically investigated in the 5–40 THz band based on Dirac semimetal and VO<sub>2</sub> strips. Two absorption peaks (the amplitudes are 76% and 60% at resonance frequencies 10.1 THz and 20.3 THz) are obtained at room temperature. Three regulation methods are suggested (temperature, Fermi energy, and magnetic field) based on the tunable properties of the Dirac semimetal and VO<sub>2</sub> strips. Both of the P1 and P2 are enhanced and shifted to higher frequencies with the Fermi energy increasing. Three newly absorption peaks (P3, P4, and P5) are achieved and shifted to lower frequencies with the temperature increasing, while the P1 and P2 are insensitive to temperature. Two newly absorption peaks (P6 and P7) are revealed and shifted to higher frequencies with the magnetic field strength increasing. The P1 is also enhanced and shifted to higher frequencies with the magnetic field strength increasing, while the P2 is not sensitive to magnetic field strength. The proposed metamaterial absorber reveals the tunable in the 5–40 THz band and the convertibility of the resonant properties, which can be applied in many important applications, including sensing or terahertz switching devices.

#### Acknowledgments

This research was financially supported by the Doctor's Scientific Research Foundation (No. HZUBS201503), the Young and Middle Teachers' Basic Ability Improvement Project of Guangxi (No. KY2016YB453), the Mathematical Support Autonomous Discipline Project of Hezhou University (No. 2016HZXYSX01), and the Innovation and Entrepreneurship

Students Project of Hezhou University (Nos. 201611838018, 201911838062, 201911838071, 201911838179).

## ORCID iDs

Min Zhong  <https://orcid.org/0000-0002-0301-8324>

## References

- [1] Ramakrishna S A 2005 Physics of negative refractive index materials *Rep. Prog. Phys.* **68** 449–521
- [2] Zhang X and Liu Z 2008 Superlenses to overcome the diffraction limit *Nat. Mater.* **7** 435–41
- [3] Schurig D, Mock J J, Justice B J, Cummer S A, Pendry J B, Starr A F and Smith D 2006 Metamaterial electromagnetic cloak at microwave frequencies *Science* **314** 977–80
- [4] Mezzapesa F P, Columbo L L, Rizza C, Brambilla M, Ciattoni A, Dabbicco M, Vitiello M S and Scamarcio G 2015 Photo-generated metamaterials induce modulation of CW terahertz quantum cascade lasers *Sci. Rep.* **5** 16207–14
- [5] Li Y, Yu G, Liang B, Zou X, Li G, Cheng S and Cheng J 2014 Three-dimensional ultrathin planar lenses by acoustic metamaterials *Sci. Rep.* **4** 6830–5
- [6] Kapitanova P V, Ginzburg P, Rodríguez-Fortuño F J, Filonov D S, Voroshilov P M, Belov P A, Poddubny A N, Kivshar Y S, Wurtz G A and Zayats A V 2014 Photonic spin Hall effect in hyperbolic metamaterials for polarization-controlled routing of subwavelength modes *Nat. Commun.* **5** 3226–33
- [7] Cheng C W, Abbas M N, Chiu C W, Lai K T, Shih M H and Chang Y C 2012 Wide-angle polarization independent infrared broadband absorbers based on metallic multisized disk arrays *Opt. Express* **20** 10376–81
- [8] Pang Y Q, Wang J F, Ma H, Feng M D, Li Y F, Xu Z, Xia S and Qu S B 2016 Spatial k-dispersion engineering of spoof surface plasmon polaritons for customized absorption *Sci. Rep.* **6** 29429
- [9] Pitchappa P, Ho C P, Kropelnicki P, Singh N, Kwong D L and Lee C K 2014 Dual band complementary metamaterial absorber in near infrared region *J. Appl. Phys.* **115** 193109–14
- [10] Andryieuski A and Lavrinenko A I V 2013 Graphene metamaterials based tunable terahertz absorber: effective surface conductivity approach *Opt. Express* **21** 9144–55
- [11] Chen X, Chen X, Wu Z, Zhang Z, Wang Z, Heng L, Wang S, Zou Y and Tang Z 2018 An ultra-broadband and lightweight fishnet-like absorber in microwave region *J. Phys. D: Appl. Phys.* **51** 285002
- [12] Wu Z, Chen X, Zhang Z, Heng L, Wang S and Zou Y 2019 Design and optimization of a flexible water-based microwave absorbing metamaterial *Appl. Phys. Express* **12** 057003
- [13] Wu Z, Chen X, Zhang Z, Heng L, Wang S and Zou Y 2019 Impedance matching for omnidirectional and polarization insensitive broadband absorber based on carbonyl iron powders *J. Magn. Magn. Mater.* **476** 349–54
- [14] Yin X, Schaferling M, Michel A U, Tittl A, Wuttig M, Taubner T and Giessen H 2015 Active chiral plasmonics *Nano Lett.* **15** 4255–60
- [15] Miao Z, Wu Q, Li X, He Q, Ding K, An Z, Zhang Y and Zhou L 2014 Widely tunable terahertz phase modulation with gate-controlled graphene metasurfaces *Phys. Rev. X* **5** 041027
- [16] Zhu W M, Liu A Q, Bourouina T, Tsai D P, Teng J, Zhang X, Lo G Q, Kwong D L and Zheludev N I 2012 Microelectromechanical Maltese-cross metamaterial with tunable terahertz anisotropy *Nat. Commun.* **3** 1274
- [17] Buchnev O, Podoliak N, Kaczmarek M, Zheludev N I and Fedotov V A 2015 Electrically controlled nanostructured metasurface loaded with liquid crystal: toward multifunctional photonic switch *Adv. Opt. Mater.* **3** 674–9
- [18] Zhou J, Chowdhury D R, Zhao R, Azad A K, Chen H, Soukoulis C M, Taylor A J and Ohara J F 2012 Terahertz chiral metamaterials with giant and dynamically tunable optical activity *Phys. Rev. B* **86** 035448
- [19] Zhang H-T, Zhang L, Mukherjee D, Zheng Y-X, Ryan C H, Alem N and Engel-Herbert R 2015 Wafer-scale growth of VO<sub>2</sub> thin films using a combinatorial approach *Nat. Commun.* **6** 8475–82
- [20] Seal K, Sharoni A, Messman J M, Lokitz B S, Shaw R W, Schuller I K, Snijders P C and Thomas Z W 2014 Resolving transitions in the mesoscale domain configuration in VO<sub>2</sub> using laser speckle pattern analysis *Sci. Rep.* **4** 6259–65
- [21] Timusk T, Carbotte J P, Homes C C, Basov D N and Sharapov S G 2013 Three-dimensional Dirac fermions in quasicrystals as seen via optical conductivity *Phys. Rev. B* **87** 235121
- [22] Shekhar C *et al* Extremely large magnetoresistance and ultrahigh mobility in the topological Weyl semimetal candidate NbP *Nat. Phys.* **11** 645–92015
- [23] Liu Z K *et al* A stable threedimensional topological Dirac semimetal Cd<sub>3</sub>As<sub>2</sub> *Nat. Mater.* **13** 677–812014
- [24] Wang J, Chen Y, Chen X, Hao J, Yan M and Qiu M 2011 Photothermalreshaping of gold nanoparticles in a plasmonic absorber *Opt. Exp.* **19** 14726–34
- [25] Hua Y and Li Z 2009 Analytic modal solution to transmission and collimation of light by one-dimensional nanostructured subwavelength metallic slits *J. Appl. Phys.* **105** 013104
- [26] Hua Y L and Li Z Y 2009 Analytic modal solution to transmission and collimation of light by one-dimensional nano-structured subwavelength metallic slits *J. Appl. Phys.* **105** 013104–7
- [27] Smith D R, Schult S, Markos P and Soukoulis C M 2002 Determination of effective permittivity and permeability of metamaterials from reflection and transmission coefficients *Phys. Rev. B* **65** 195104–8
- [28] Hood P J and DeNatale J F 1991 Millimeter-wave dielectric properties of epitaxial vanadium dioxide thin films *J. Appl. Phys.* **70** 376–81
- [29] Rozen J, Lopez R, Haglund R F Jr and Feldman L C 2006 Two-dimensional current percolation in nanocrystalline vanadiumdioxide films *Appl. Phys. Lett.* **88** 081902
- [30] Smith N V 2001 Classical generalization of the Drude formula for the optical conductivity *Phys. Rev. B* **64** 155106
- [31] Kotov O V and Lozovik Y E 2016 Dielectric response and novel electromagnetic modes in three-dimensional Dirac semimetal films *Phys. Rev. B* **93** 235417
- [32] Timusk T, Carbotte J P, Homes C C, Basov D N and Sharapov S G 2013 Three-dimensional Dirac fermions in quasicrystals as seen via optical conductivity *Phys. Rev. B* **87** 235121
- [33] Ding P, Liang E, Cai G, Hu W, Fan C and Xue Q 2011 Dual-band perfect absorption and field enhancement by interaction between localized and propagating surface plasmons in optical metamaterials *J. Opt.* **13** 075005
- [34] Kreibitz U and Vollmer M 1995 *Optical Properties of Metal Clusters* (Berlin: Springer) 978-3-642-08191-0 (<https://doi.org/10.1007/978-3-662-09109-8>)
- [35] Yao Y, Kats M A, Genevet P, Yu N, Song Y, Kong J and Capasso F 2013 Broad electrical tuning of graphene-loaded plasmonic antennas *Nano Lett.* **13** 1257–64

- [36] Hwang J and Roh J W 2017 Electrically tunable two-dimensional metasurfaces at near-infrared wavelengths *Opt. Express* **25** 25071–8
- [37] Li Z and Yu N 2013 Modulation of mid-infrared light using graphene-metal plasmonic antennas *Appl. Phys. Lett.* **102** 131108
- [38] Gorbar E V, Miransky V A and Shovkovy I Chiral anomaly, dimensional reduction, and magnetoresistivity of Weyl and Dirac semimetals *Phys. Rev. B* **89** 085126
- [39] Zyuzin A A, Hook M D and Burkov A A 2011 Parallel magnetic field driven quantum phase transition in a thin topological insulator film *Phys. Rev. B* **83** 245428
- [40] Al'tshuler B L and Aronov A G 1981 Magnetoresistance of thin films and of wires in a longitudinal magnetic field *JETP Lett.* **33** 499
- [41] Burkov A A 2015 Negative longitudinal magnetoresistance in Dirac and Weyl metals *Phys. Rev. B* **91** 245157